






Orbital angular momentum-based dual-comb interferometer for ranging and rotation sensing

ALEXANDER Q. ANDERSON,^{1,*}  ELIZABETH F. STRONG,² 
SEAN C. COBURN,² GREGORY B. RIEKER,²
AND JULIET T. GOPINATH^{1,3} 

¹*Department of Electrical, Computer, and Energy Engineering, University of Colorado, Boulder, CO 80309, USA*

²*Department of Mechanical Engineering, University of Colorado, Boulder, CO 80309, USA*

³*Department of Physics, University of Colorado, Boulder, CO 80309, USA*

*alexander.q.anderson@colorado.edu

Abstract: We present a dual-comb interferometer capable of measuring both the range to a target as well as the target's transverse rotation rate. Measurement of the transverse rotation of the target is achieved by preparing the probe comb with orbital angular momentum and measuring the resultant phase shift between interferograms, which arises from the rotational Doppler shift. The distance to the target is measured simultaneously by measuring the time-of-flight delay between the target and reference interferogram centerbursts. With 40 ms of averaging, we measure rotation rates up to 313 Hz with a precision reaching 1 Hz. Distances are measured with an ambiguity range of 75 cm and with a precision of 5.9 μm for rotating targets and 400 nm for a static target. This is the first dual-comb ranging system capable of measuring transverse rotation of a target. This technique has many potential terrestrial and space-based applications for lidar and remote sensing systems.

© 2022 Optica Publishing Group under the terms of the [Optica Open Access Publishing Agreement](#)

1. Introduction

Laser remote sensing, especially light detection and ranging (lidar) technologies are becoming increasingly widespread due to their ability to precisely measure distance and velocity. These technologies are enabling diverse applications in identifying and tracking remote targets for navigation, metrology, atmospheric and Earth sciences, and medicine and biological measurements [1–9]. Continuous wave interferometry can provide measurements with sub-nanometer precision for applications requiring extremely precise measurements of changes in distance, such as metrology, intersatellite ranging, or even detecting gravitational waves [4,10,11]. However, these systems only measure relative changes in distance of up to half the optical wavelength. In contrast, pulsed and frequency-modulated lidars can measure distances on the scale of meters or kilometers for applications that require a more modest resolution down to tens of microns [6,7,12,13]. While these traditional techniques typically compromise either resolution or range, dual-comb interferometry offers a method to achieve sub-micron precision with a long ambiguity range simultaneously [14–17]. This technique, known as dual-comb ranging (DCR), uses a pair of mutually coherent optical frequency combs with slightly different repetition rates. The signal comb interrogates the target then interferes with the local oscillator comb; this employs linear optical sampling to down-convert the interference signal from the optical domain to the radio-frequency domain to produce a cross-correlation signal with effective time-steps of less than 1 ps [14,18–20]. With minimal averaging time (10 ms), these systems can provide absolute measurements of kilometer-scale distances to a precision of less than 10 nm [15,16]. The combination of both high precision and a long ambiguity range has led to proposals of applying DCR to inter-satellite ranging [14], large-scale manufacturing [14,19], and other 3-dimensional imaging and lidar applications [18–20]. Recent advances have increased the robustness and

practicality of DCR by enabling measurements of non-cooperative (scattering) targets [21], reducing the ranging sensitivity to variations in the air's refractive index [22], lowering the high data burdens and increasing the acquisition rates [23], and enabling a compact form factor with micro-resonator based frequency combs for DCR [24].

Ranging techniques offer several solutions to measuring the distance and longitudinal velocity of a target; however, many targets have additional degrees of freedom, such as rotation, which must also be measured to fully characterize the system. For instance, satellite tracking systems use combinations of lidar for longitudinal rotation and position measurements supplemented with imaging with computer vision to track spin-stabilized satellites and tumbling space debris in order to track their orientation, calculate the evolution of their orbits to avoid collisions and provide course corrections, and to help eliminate space debris [12,25–28]. In terrestrial applications, the range and rotation rate can be measured to help identify projectiles and predict their trajectories [29]. On a smaller scale, ranging and rotation measurements may be used to study turbulent fluids for applications such as combustion or biological systems [30,31]. Currently, measuring a target's transverse rotation in addition to its range requires either making multiple lateral measurements and calculation of the solid body rotation [5,12,32], or the addition of a second separate measurement modality [33,9]. Here, we demonstrate a novel dual-comb ranging system which simultaneously measures the distance to the target and the transverse rotation of the target by measuring the rotational Doppler shift.

Analogous to the more familiar linear Doppler shift which is proportional to a target's longitudinal velocity, the rotational Doppler shift (RDS) describes the frequency shift arising from a relative rotation transverse to the light beam and is proportional to the change in the orbital angular momentum (OAM) of the light [34,35]. OAM in light is characterized by helical wavefronts, described by phase $e^{i\ell\phi}$, where ℓ is the topological charge and ϕ is the azimuthal angle [36]. For a change of $\Delta\ell h$ in the OAM of light scattered from a target rotating with angular frequency of Ω , the rotational Doppler shift $\Delta\omega$ is given by Eq. (1) [35,37]:

$$\Delta\omega = \Delta\ell\Omega \quad (1)$$

The rotational Doppler shift has been proposed for measuring rotation and vorticity in fluids [38–41], astronomical bodies [42], rotational vibrations [43], very slowly rotating objects [44,45], and remote rotating objects [46]. Additionally, extensions of the RDS to measure other transverse motion trajectories have been proposed by further adapting spatial phase profiles of the structured light [47,48]. In 2014, a system was demonstrated to measure both rotational velocity and longitudinal velocity by switching between Gaussian and OAM illumination [9]; however, this technique only measured motion without ranging. Our dual-comb interferometer measures both range and rotation simultaneously with a single illumination mode.

We present the operating principle in Sec. 2, followed by the details of our experimental setup in Sec. 3. The results of measuring the range and rotation of the target are presented in Sec. 4. Finally, in Sec. 5 we conclude with a discussion of strategies to further improve the precision and extend the limits of our system.

2. Theoretical framework

A dual-comb ranging interferometer uses two coherent frequency combs with repetition rates f_{r1} and f_{r2} , with a difference in repetition rates of Δf_{rep} . The signal comb is sent through a Michelson interferometer, sampling a reference mirror in one arm and the target in the second arm, as seen in Fig. 1 [14]. The returned signal is heterodyned with the local oscillator (LO) comb on a photodetector to produce an interferogram, the optical cross-correlation of the two pulse trains, by linear optical sampling [14,18,20,49]. The resulting interferogram (Fig. 2) consists of two centerbursts (or envelopes of interference fringes), corresponding to the reference and target

reflections. The interferograms have an update period of τ and have N measurement points separated by an effective time step of δt , as described in Eq. (2) [20].

$$\tau = 1/\Delta f_{rep} \quad (2a)$$

$$\delta t = \frac{\Delta f_{rep}}{f_{r1}f_{r2}} \quad (2b)$$

$$N = \frac{f_{r1}}{\Delta f_{rep}} \quad (2c)$$

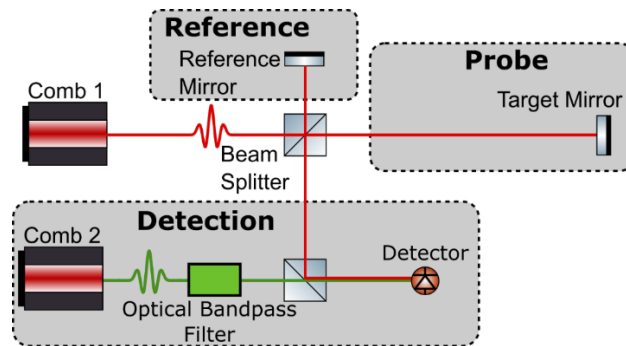


Fig. 1. Generalized schematic of dual-comb ranging interferometer (without rotation sensing). Comb 1 emits the probe pulse train, which is split between the reference and target arms. The reflected light returns to the beamsplitter and combines with comb 2 on the detector. The optical bandpass filter in comb 2 is used to reduce the comb bandwidth to achieve Nyquist sampling.

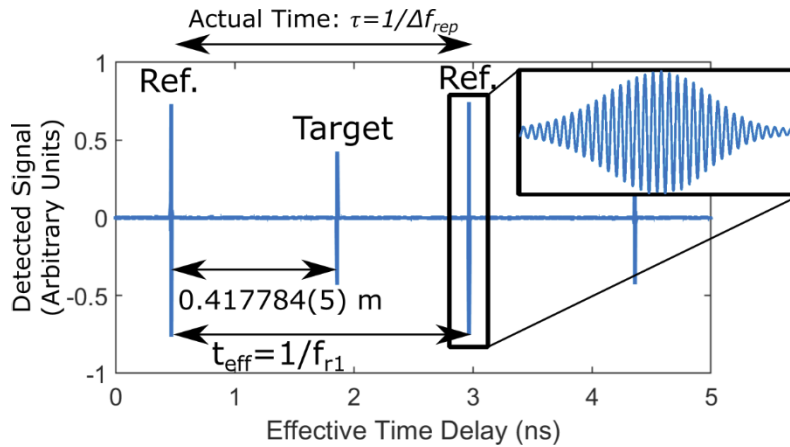


Fig. 2. Example interferogram signal from dual-comb interferometer. Two full interferogram periods are shown, with the reference (Ref.) and target centerbursts. Inset shows zoomed in example of interference fringes within the reference centerburst. The distance between the centers of the reference and target envelopes gives the range information, 0.417784 m with an uncertainty of 5 μ m in this example.

When an interferogram is recorded, the following procedure is used to measure the distance between the reference and target. The magnitude of the Hilbert transformed interferogram

removes the carrier frequency and leaves only the envelope of the signal. A series of Gaussians are fit to the remaining centerburst envelopes to find the centers of the reference and target peaks. The distance between the reference and target objects is then measured as the effective time delay of the respective centerbursts in the interferogram [16,17]. This effective time delay Δt may be simply converted to a distance as in Eq. (3), where the factor of two accounts for the round trip path length and v_g is the group velocity of the optical pulse which was approximated here as the speed of light, c .

$$d = \frac{v_g \Delta t}{2} \quad (3)$$

The interferogram period and effective time step may likewise be converted to the maximum measurable distance, or ambiguity range R , and the effective distance step δz (Eq. (4)).

$$R = \frac{v_g}{2f_{r1}} \quad (4a)$$

$$\delta z = \frac{v_g \delta t}{2} = \frac{v_g \Delta f_{rep}}{2f_r^2} \quad (4b)$$

This provides a coarse time of flight measurement on the order several microns for a single shot measurement, and this precision may be enhanced through averaging multiple measurements [14,16,17]. We note that in some applications, the precision of dual comb ranging measurements is further enhanced by utilizing the optical carrier phase [14–16]; however, the carrier phase in our system is instead used for measuring the transverse rotation of the target.

Measurement of the transverse rotation of the target is achieved by utilizing the rotational Doppler shift. Prior to the target, the signal comb is prepared with $\ell \hbar$ of OAM. The light is then launched to a rotating target, aligned to the rotation axis of the target. The target is designed with particular topological charges in order to impart a torque of $-2 \ell \hbar$ to the reflected light. Note that light may be returned in many OAM modes, but as discussed in Sec. 3, our system is mode-selective and measures only light scattered into the $-\ell$ mode. Therefore, a variety of different targets may be used [50,51], including a retroreflector [52], one or more scattering particles [9,53], a randomly scattering surface [37], a petal or clover-shaped target [46], or an OAM-based hologram [54]. When the signal pulse returns from the target, the $-\ell$ mode is converted back to $\ell = 0$ via a forked grating and coupled into single mode fiber so it can interfere with the LO. The carrier phase of the target signal is obtained from the phase of the Hilbert transform of the interferogram, so that the phase shift $\Delta \phi$ between consecutive interferograms can be measured. The phase shift between interferograms is proportional to both change in distance Δz and transverse rotation rate, f_{rotate} , as shown in Eq. (5), where τ is the interferogram period calculated from Eq. (2a).

$$\Delta \phi = 2\pi \left(\frac{2n\Delta z}{\lambda} + \Delta \ell f_{rotate} \tau \right) \pmod{2\pi} \quad (5)$$

We assume the distance to the target does not change over the course of the measurement, so any change in the carrier phase between consecutive interferograms may be attributed to the rotational Doppler shift. The phase shift between interferograms, wrapped between $-\pi$ and π , is used to calculate the rotational frequency of the target.

$$f_{rotate} = \frac{\Delta \phi}{2\pi \tau \Delta \ell} \quad (6)$$

To achieve Nyquist sampling limits and properly sample the full signal envelope, the optical bandwidth of the comb pulses $\Delta \nu$ must be filtered ensuring that the effective time steps are much

less than the pulse width [17,55].

$$\Delta\nu < \frac{1}{2\delta t} = \frac{f_{r1}f_{r2}}{2\Delta f_{rep}} \quad (7)$$

While this first condition is the minimum sampling requirement for any dual comb interferometry measurement, a second more restrictive requirement is needed in order to process the data with a Hilbert transform (or other data processing techniques). It is necessary to further restrict the pulse bandwidth or adjust the effective time steps by modifying the combs' repetition rates to ensure that there are at minimum two complete fringes within the coherence length in order for the Hilbert transform to successfully measure the phase of the carrier [17,56,57]. An alternative, less restrictive approach would be to use in-phase/quadrature (IQ) detection to relax this constraint [17,57]; however, IQ detection requires a more complex optical design and calibration as well as at least one additional detector [57–59].

Due to the cyclic nature of phase measurements, there exists a maximum rotation rate for which the rotation can be measured without aliasing. This will be referred to here as the *rotation ambiguity limit* and is described as:

$$-\frac{1}{2\tau\Delta\ell} < f_{rotate} < \frac{1}{2\tau\Delta\ell} \quad (8)$$

If the rotation ambiguity limit is too restrictive to measure the desired rotation rate and it is not possible to sufficiently adjust τ , the Chinese remainder theorem (CRT) may be used to further extend the ambiguity limit as described below [60–62]. Due to phase wrapping, measuring a rotation rate \hat{f} which is greater than the rotation ambiguity limit results in a directly calculated rotation rate f' modulo $1/(\tau\Delta\ell)$, as

$$f' = \frac{\Delta\phi}{2\pi} \left(\frac{1}{\tau\Delta\ell} \right) \equiv \hat{f} \left(\text{mod} \frac{1}{\tau\Delta\ell} \right) \quad (9)$$

The ambiguity may be resolved by making K measurements with different OAM states (and/or different τ), and solving the following system of Diophantine equations [61], (however, this does require a priori knowledge of the direction of rotation).

$$\hat{f} = m_i \left(\frac{1}{\tau_i\Delta\ell_i} \right) + f'_i, \quad i = 1, 2, \dots, K \quad (10a)$$

$$\text{where } 0 \leq m_i \leq \hat{f}_{max} \times (\tau_i\Delta\ell_i) \quad (10b)$$

The maximum rotation rate, \hat{f}_{max} , which may be measured with CRT is the least common multiple of all $\tau\Delta\ell_i$. For simplicity, the maximum likelihood (ML) method is implemented to solve the set of equations, searching all possible combinations of m_i to minimize the variance of the K calculated rotation rates, \hat{f}_i [61]. The ML estimation is the mean of all resulting \hat{f}_i . A simple demonstration of the CRT is implemented here as a proof of concept, but more work is likely required to better optimize its application to this measurement.

3. Experimental setup

The lasers used here are erbium-doped all-polarization-maintaining fiber frequency combs with a linear-cavity design and a semiconductor saturable absorber mirror (SESAM) to achieve passive mode-locking [63,64]. The combs are centered at ~1560 nm with repetition rates of approximately 200.013 MHz, and a difference in repetition rates Δf_{rep} of 626.7 Hz. Note that the repetition rates could be further optimized to improve ranging accuracy [56], to adjust the ambiguity range [14], or to adjust the rotation ambiguity limit. The carrier envelope offset frequency of each comb is locked via a standard f-2f method, and the repetition rates are stabilized

through a phase lock of a single tooth from each comb to a stable, narrow linewidth continuous wave laser [65,66]. The optical spectra of both lasers are initially filtered with a 40 nm bandpass filters centered at 1550 nm; however, the optical bandwidth of the local oscillator comb is further reduced with a 0.55 nm bandpass filter at 1550 nm to meet the sampling requirements previously discussed (Fig. 3). Following these filters, the signal comb has a power of 17.65 dBm, and the local oscillator comb has a power of -10.30 dBm.

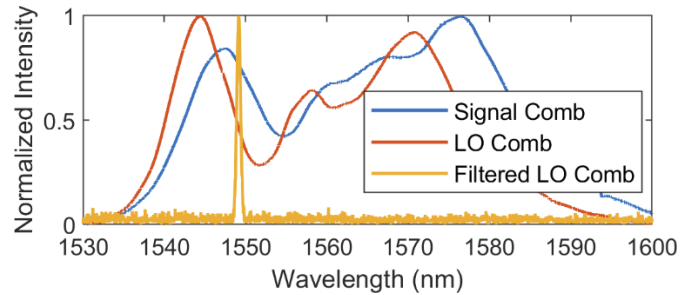


Fig. 3. Optical spectra of signal comb and local oscillator (LO) comb. While both lasers are initially filtered with a 40 nm bandpass filter, the local oscillator comb is further filtered by a tunable optical bandpass filter at 1550 nm, as shown in yellow to achieve Nyquist sampling and reduce the effects of dispersion.

The Δf_{rep} of the combs sets the rotation ambiguity limit corresponding to each measured $\Delta \ell$ (Eq. (8)); Fig. 4 illustrates this restriction. As can be seen, smaller OAM values allow for the measurement of faster rotation rates, while measurements with large OAM values are limited to measuring slower rotation rates. Note that $\Delta \ell$ must be a non-zero integer because OAM states are discrete integers, and a $\Delta \ell$ of 0 would not result in a rotational Doppler shift (as seen by Eq. (1)). For each measured dataset in this paper (except the data for the Chinese remainder theorem which extends this rotation ambiguity limit through signal processing), care is taken to keep the true rotation rate below this limit to allow for an accurate calculation of the rotation.

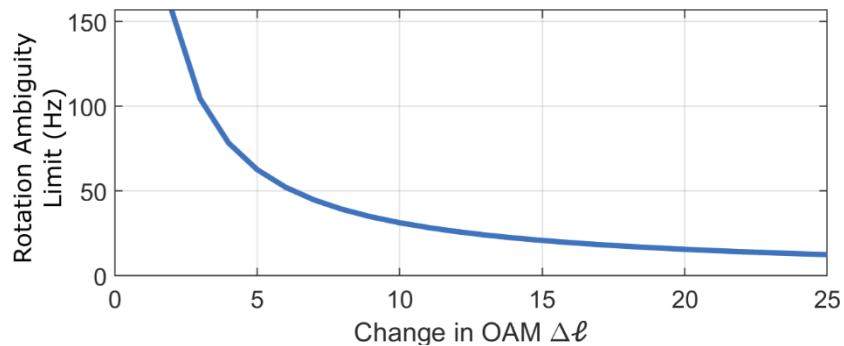


Fig. 4. Rotation ambiguity limit versus the change in OAM used for detection. This plot is calculated from Eq. (8). Note that using smaller OAM values allow for measuring faster rotation rates, and larger OAM is limited to measuring slower rotation rates.

The experimental schematic for the dual-comb range and rotation sensing interferometer is shown in Fig. 5. The primary change in this interferometer compared to the generic dual-comb ranging interferometer of Fig. 1 is the generation of OAM in the probe arm, as will be described below. One additional change is an attenuator is added to the reference arm in order to approximately match the returned power from the reference and probe arms.

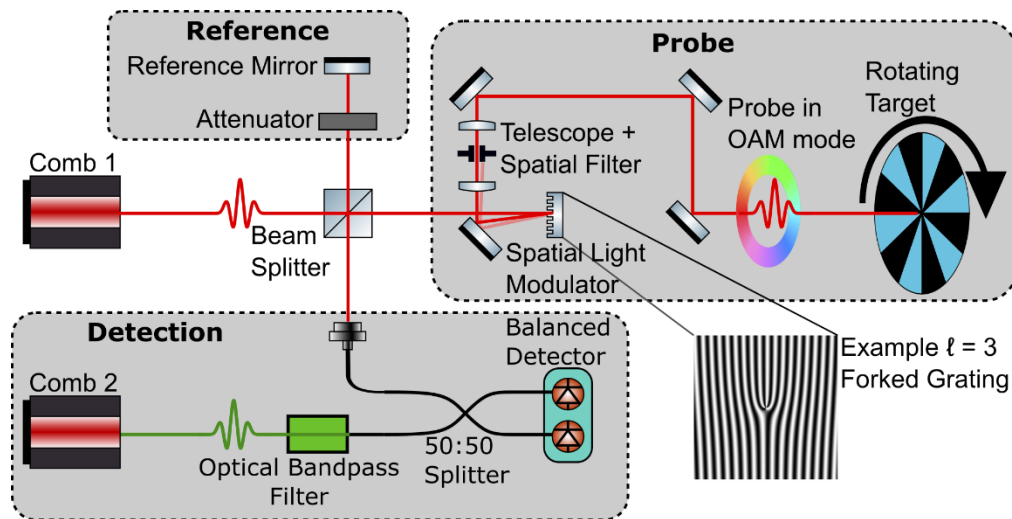


Fig. 5. Experimental schematic of dual-comb ranging and rotation sensing interferometer. Comb 1 emits the probe pulse train, which is split between the reference and target arms. In the target arm, a spatial light modulator (SLM) prepares the probe in an orbital angular momentum (OAM) mode of $+\ell$ using a forked grating. A telescope is used to spatially filter the beam to select the proper diffracted mode from the SLM, and the probe is launched onto the target. The backscattered light from the target returns to the SLM where its OAM state is again incremented by $+\ell$ and the probe is coupled into single mode fiber where it is combined with comb 2 on the balanced detector.

In the probe arm of the interferometer, the probe beam is first prepared with OAM using a spatial light modulator (SLM, Meadowlark Optics), using a forked grating of order ℓ which generates a hypergeometric gaussian (HyGG) beam of $\ell\hbar$ OAM in the first diffracted mode. A spatial filter is used to select the desired diffracted mode, which is then sent to the target. Light backscattered from the target returns to the forked grating on the SLM, which will again add $\ell\hbar$ of OAM to the light before the light is coupled in single mode fiber (SMF). This alignment is achieved by aligning the detection optics to the launch optics. Because light with nonzero OAM does not couple into SMF, the SLM and fiber acts as a modal filter for $\ell = 0$ on the returning light, ensuring that any measured light must have been converted from a $+\ell$ OAM state to a $-\ell$ state by the target. This ensures only a single rotational Doppler shift harmonic is measured [34]. Additionally, this optical geometry dictates that the measured $\Delta\ell$ will always be -2ℓ . Following this modal filtering step, the signal comb is combined with the reference in a 50:50 splitter and measured on a 100 MHz balanced detector (Koheron PD100B). The signal from the detector is low pass filtered (Mini-Circuits SLP-50+, DC-48 MHz) and recorded with a data acquisition system (National Instruments 7965 FPGA and 5761 Digitizer).

The rotating target for this proof of concept was simulated using an SLM in order to eliminate the mechanical vibrations from physically rotating a target, which can introduce ambiguity into the measurements (see Eq. (5)). The SLM displays a blazed grating in Littrow configuration so that the probe is reflected back to the detector, and a structured target is added to this grating. A desired target phase and amplitude can be achieved by first adding the desired phase to the blazed grating; the desired amplitude modulation can be achieved by modulating the depth of the phase profile of the grating [67]. In order to simulate rotation, the target on the SLM is rotated while the blazed grating remains stationary [41]. Because the SLM refresh rate is much slower than the

interferogram refresh rate of τ , a “stop motion” scheme is used in which each SLM frame is advanced $2\pi f_{rotate}\tau$ radians and is measured with a single interferogram, frame-by-frame.

One example target we desired to simulate was a retroreflector, as such a reflector imparts a torque of $-2\ell\hbar$ to incident OAM modes as required [52]. To simplify representing a retroreflector with an SLM, this target was simulated functionally by using a forked grating of -2ℓ for an incident mode of ℓ . Other targets are also used, such as a spoke pattern demonstrating an amplitude only target, or a target consisting of the sum of several forked gratings; the specific targets used are shown in the following section.

4. Results

As described above, the rotation rates of a several different spinning targets were measured using various incident OAM states ℓ , corresponding to $\Delta\ell = -2\ell$ due to the optical geometry as explained above. For consistency, each measurement uses 40 ms of averaging, corresponding to 25 interferograms at a Δf_{rep} of 626.7 Hz. This averaging time is comparable to that used in other dual-comb ranging experiments [14,16,17]. The position and rotation rate of the target is calculated for all measured interferograms.

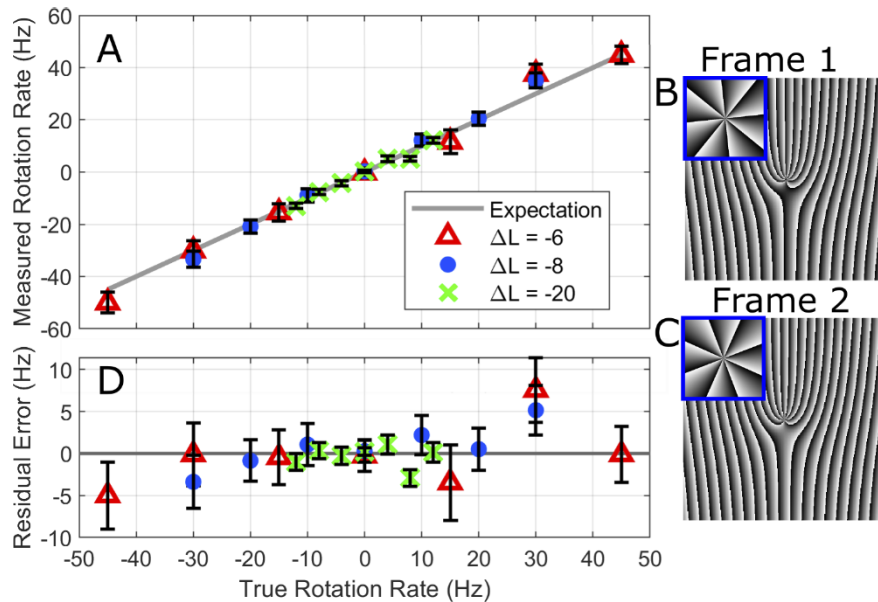


Fig. 6. (A) Measured rotation vs true rotation rate using forked grating as target, with residual error shown in (D). Error bars are standard error of the mean for 25 interferograms, with a mean uncertainty of 3.5, 2.5, and 1 Hz for $\Delta\ell$ of -6 , -8 , and -20 , respectively. (B) Example of single frame of rotating forked grating for $\Delta\ell = 8$; inset shows spiral phase which was added to the stationary blazed grating. Grating period increased here for visualization. (C) Second frame of rotating target.

We first demonstrate rotation measurements using a forked grating target (Fig. 6). The position of the targets remained the same for all of these rotation conditions, and was consistently measured in the interferograms as approximately 0.417770 m. The accuracy of the ranging measurements will be discussed at the end of this section. Both negative and positive rotation rates are well predicted, with average uncertainties of 3.5, 2.5 and 1 Hz for $\Delta\ell$ of -6 , -8 , and -20 , respectively. While all measurements accurately measure the rotation, it is worth noting that measurements using higher OAM values result in better precision. This higher precision

arises because equal levels of phase noise are scaled down by a factor of $1/\Delta\ell$ when converting the phase measurement to a rotation rate. This scaling rule is plotted in Fig. 7. The average phase noise of these measurements was used to calculate the expected precision in measuring the rotation rate. The mean uncertainty from each rotation dataset presented in this paper was then plotted, which shows good agreement with the calculated trend for expected precision. While the highest measured precision for the target's rotation rate is 1 Hz, Fig. 7 demonstrates that increasing the OAM of the probe continues to improve the precision.

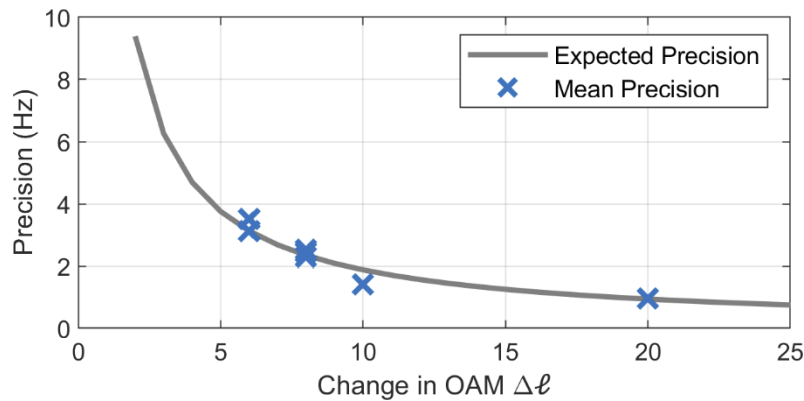


Fig. 7. Precision vs change in OAM $\Delta\ell$ used for detection. The expected precision is calculated based on the mean phase noise measured in all rotation datasets. The mean precision values are the average precision of the rotation measurement for each rotation dataset presented. The precision for all datasets is calculated as the standard error of the mean calculated rotation rate using 25 interferograms.

Additional rotation measurements were made using different types of targets, as shown in Fig. 8. Despite these new targets having a greater distribution of topological charges and thus scattering light into a broader set of OAM modes, there is no degradation in the rotation measurement precision. A target consisting of rotating spokes demonstrated measurement using an amplitude-only target. Additionally, a target composed of the sum of topological charges $\ell = 6, 8,$ and -10 spiral phase patterns was measured using incident illumination first of ℓ of 3, followed by ℓ of -5 . These measurements demonstrate that a generalized target with several topological charges may be used without degradation of the measurement; different OAM illumination states do not require unique targets.

Next, the Chinese remainder theorem is demonstrated in measuring targets rotating faster than the rotation ambiguity rate. Consecutive measurements of a rotating target are made with OAM illumination ℓ of 3, 4, and 5. For these OAM states, the highest ambiguity rate is 52.2 Hz, and the target is set to spin at rates of 125, 200, and 245 Hz. As seen in Fig. 9, these rotation rates were all measured accurately with a mean uncertainty of 2.7 Hz.

To verify the accuracy of the ranging measurement, the reference mirror was translated on a linear stage to systematically increment the distance between the reference and target (Fig. 10). Measurements of both rotation and range are made at discrete steps of the translation stage at 0, 3, 6, and 9 cm. All measurements used a $\Delta\ell$ of 8. Although the full ambiguity range, as given by Eq. (4a), allows 75 cm of displacement, we were limited here by the travel of the stage. Because the translation stage provides only a known increment to the range rather than an absolute measurement, the distance here is reported as a displacement relative to the estimated start point. To account for measurement uncertainty, the start point was calculated by fitting the measured displacement data. For all distances measured, the rotation was correctly measured with a mean precision of 1.8 Hz, which is in good agreement with the rotation measurements

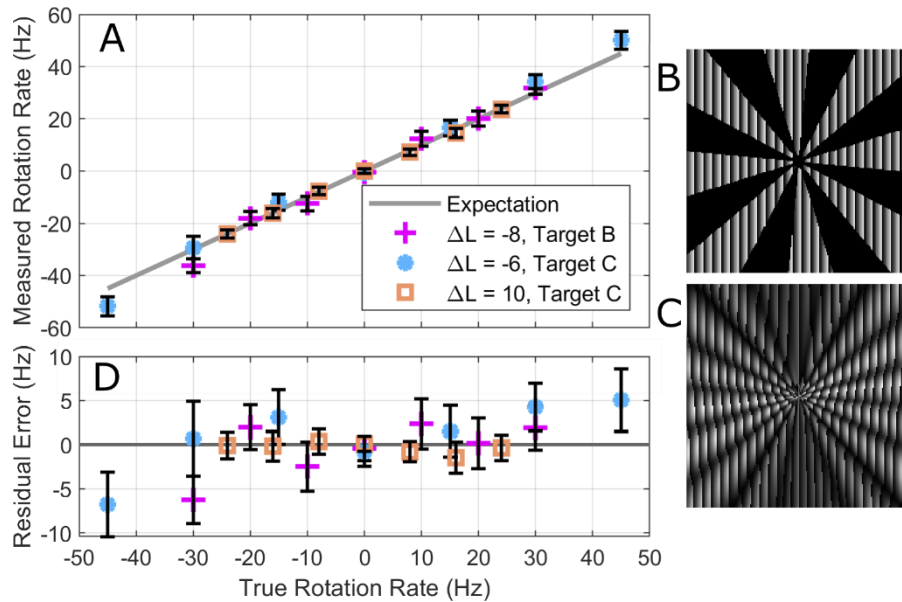


Fig. 8. (A) Measured rotation vs true rotation rate using a variety of rotating targets with multiple topological charges, with residual error plotted in (D). Error bars: standard error of the mean from 25 measured interferograms. Mean uncertainty is 2.5, 3.2, and 1.4 Hz for $\Delta\ell$ of -8, -6, and 10 respectively. Pink crosses used rotating spokes pattern shown in (B). Summed spiral pattern in (C) used for both the cyan and orange measurements.

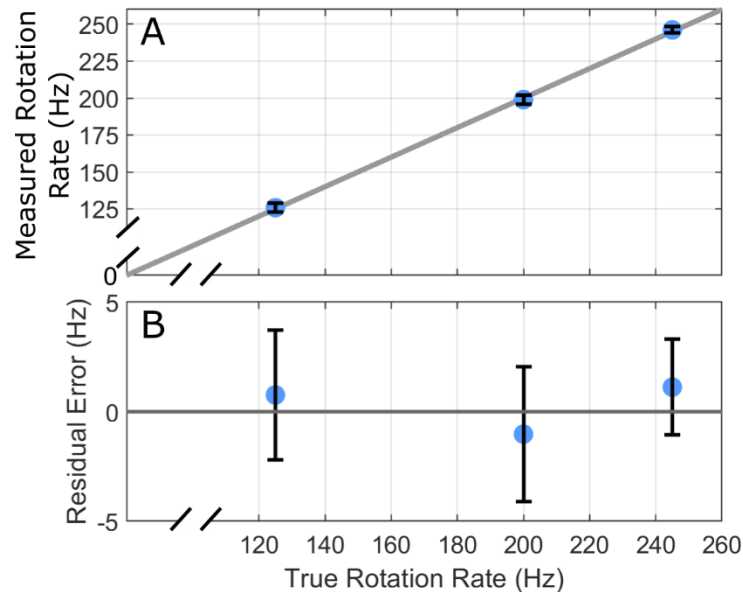


Fig. 9. (A) Measured rotation rates using the Chinese remainder theorem (CRT) vs the true rotation rate, with residual error plotted in (B). This enables a significant increase in the maximum measurable rotation rate. Each rotation rate was measured three times, using $\Delta\ell$ of 6, 8, and 10. Error bars: standard error of the mean of the CRT predicted rate from each $\Delta\ell$ measurement, average uncertainty of 2.7 Hz. Gray line represents expected rotation values.

presented above. As can be seen in Fig. 10, the range measurements for the rotating targets have greater variances, with an average standard error of the mean of $5.9\ \mu\text{m}$ for the rotating targets and $400\ \text{nm}$ for the $0\ \text{Hz}$ targets. The higher uncertainty for a rotating target may be due to a combination of possible factors, including unintentional axial target motion due to out of plane rotation arising from potential misalignment between the rotation axis and the measurement axis, other misalignment issues either with the probe or detection optics, possible imperfections in the illumination beam, or even spatiotemporal tilt on the probe due to unintentional effects from the gratings on the SLM. Regardless of the difference in precision, both the rotating and static targets accurately measure the expected incremented distance, and minor discrepancies in distance may also be attributed to the translation stage which has a specified precision of only $3.25\ \mu\text{m}$.

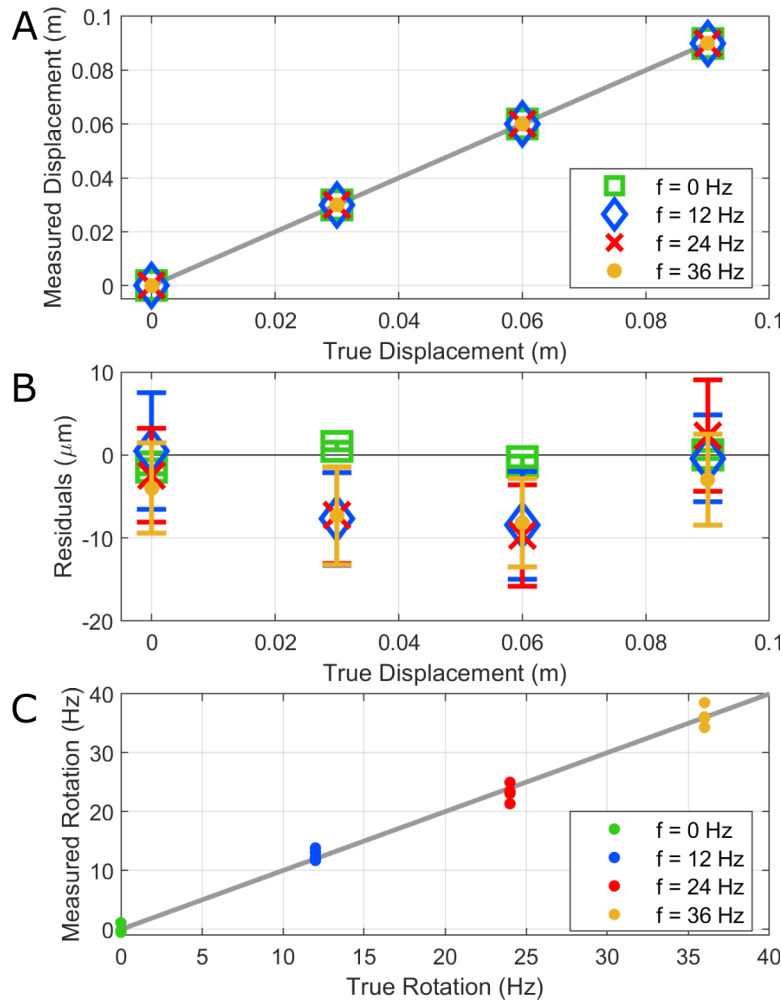


Fig. 10. Measured displacement versus true displacement from linear stage (A) and measurement residuals (B). Error bars: standard error of the mean for 25 interferograms. True displacement has uncertainty of $\pm 3.25\ \mu\text{m}$ of error as given by linear stage specifications. Because displacement is relative, the zero point is set by calculating the best fit line to the measured displacement, then subtracting the y-intercept of this line ($9.984\ \text{mm}$) from all the data. (C) Rotation measurements for each target at each distance plotted vs the true rotation rate. Measurement of rotation rate maintained the same level of precision as in previous measurements. All measurements made with $\Delta\ell$ of 8.

5. Discussion and conclusions

The data above demonstrate the ability of this dual-comb interferometer to measure both range and transverse rotation. One remaining technical challenge is to reduce the rotation measurement's high sensitivity to longitudinal motion, as described in Eq. (5). While a steady linear motion could potentially be measured and calibrated out, any longitudinal vibrations or changes in velocity would still significantly degrade any rotation measurements. One potential solution would be to measure the target simultaneously with two different OAM modes in orthogonal polarizations. Longitudinal motion would result in the same phase shift in both measurements, but transverse rotation would result in scaled phase shifts proportional to the OAM used. Thus, comparing the phase shifts in the two measurements would allow for the separation of linear and rotational components of the phase shifts. Implementation of such a system would then allow for the measurement of real-world targets. The rotation precision in this approach would also likely improve proportionally as the ranging uncertainty is reduced.

In conjunction to the design proposed above, a number of other design modifications may further improve ranging and rotation measurement precision. Somewhat trivially, Fig. 7 illustrates that further increasing the OAM in the probe would continue to improve the rotation measurement precision beyond the observed value of 1 Hz. For another straightforward improvement, a wider pulse bandwidth would provide a more narrow pulse envelope and thus decrease the uncertainty in the distance measurements; however, the bandwidth is ultimately constrained by sampling requirements as discussed previously [14]. The more restrictive bandwidth requirements, arising from the measurement of the phase with the Hilbert transform, may be relaxed if the phase is instead measured via IQ detection [17,57]. Additionally, two separated optical bands in the pulse may be used for synthetic wavelength interferometry to significantly improve the single-shot ranging precision [16]. Finally, the ranging and rotation measurements could further improve by minimizing the dual comb laser phase noise and timing jitter. The frequency combs used here exhibit moderate phase noise (typical values: 3 fs timing jitter, 3 rad and 0.23 rad integrated phase noise from 5MHz to 1 Hz for the carrier envelope offset frequency and optical heterodyne frequency, respectively [63]). A number of approaches for reducing phase noise have been proposed [68–72], and intrinsically lower phase noise comb sources exist [73–75].

While the Chinese remainder theorem was successfully demonstrated, the current experimental design is limited to a maximum rotation rate of $1/(2\tau)$, regardless of the OAM states used. In our experiment, this limit is approximately 313 Hz. This limit arises because all rotation measurements here implement a $\Delta\ell$ of $-2\ell_{\text{incident}}$, and all the measurements are scaled by the same $1/\tau$. An optimal system would allow for changing the interferogram period τ by using a tunable repetition rate [15], and would split the optical path to use a unique modal filter on the detection path to allow measurement of arbitrary $\Delta\ell$. This would allow the realization of the full potential of the CRT by allowing the use of truly coprime scaling factors to be implemented.

In conclusion, this OAM-based dual comb interferometer uses time of flight and the rotational Doppler shift to measure both distance to a target and transverse rotation rate. With an averaging time of 40 ms, a target's rotation rate was measured with a precision reaching 1 Hz. The concurrently measured distance has a precision of approximately 5.9 μm for a rotating target, and 400 nm for a static target. We also demonstrate the application of the Chinese remainder theorem to further extend the maximum measurable non-ambiguous rotation rate. The principles of this rotation-sensing dual-comb interferometer may be applied to lidar systems in diverse terrestrial and space-based applications, such as tracking the position and orientation of satellites or other remote objects, or even measuring particles or micro-organisms within a turbulent fluid. Additionally, the rotation sensing principles demonstrated in this dual-comb interferometer may be further applied to other types of lidar or ranging systems, or even optical coherence tomography systems; and modifications to the probe's phase structure may allow sensing of arbitrary transverse motion in addition to rotation.

Funding. National Science Foundation (DGE 1650115, DMR 1553905, ECCS 1509733, ECCS 1509928, ECCS 1554704); Air Force Office of Scientific Research (FA9550-171-0224); National Defense Science and Engineering Graduate; University of Colorado Boulder Electrical, Computer and Energy Engineering Department; University of Colorado Boulder Seed Grant Program.

Acknowledgments. Brendan Heffernan, Kelvin Wagner, Jan Bartos, Shu-Wei Huang, and Mark Siemens for helpful technical discussions. Kelvin Wagner and Michael Brand for the use of various optical equipment.

Disclosures. The authors declare no conflicts of interest.

Data availability. Data underlying the results presented in this paper are not publicly available at this time but may be obtained from the authors upon reasonable request.

References

1. B. Behroozpour, P. A. M. Sandborn, M. C. Wu, and B. E. Boser, "Lidar System Architectures and Circuits," *IEEE Commun. Mag.* **55**(10), 135–142 (2017).
2. J. Moras, V. Cherfaoui, and P. Bonnifant, "A lidar perception scheme for intelligent vehicle navigation," in *2010 11th International Conference on Control Automation Robotics & Vision* (IEEE, 2010), pp. 1809–1814.
3. P. J. de Groot, "A review of selected topics in interferometric optical metrology," *Rep. Prog. Phys.* **82**(5), 056101 (2019).
4. B. P. Abbott, R. Abbott, R. Adhikari, P. Ajith, B. Allen, G. Allen, R. S. Amin, S. B. Anderson, W. G. Anderson, M. A. Arain, M. Araya, H. Armandula, P. Armor, Y. Aso, S. Aston, P. Aufmuth, C. Aulbert, S. Babak, P. Baker, S. Ballmer, C. Barker, D. Barker, B. Barr, P. Barriga, L. Barsotti, M. A. Barton, I. Bartos, R. Bassiri, M. Bastarrika, B. Behnke, M. Benacquista, J. Betzwieser, P. T. Beyersdorf, I. A. Bilenko, G. Billingsley, R. Biswas, E. Black, J. K. Blackburn, L. Blackburn, D. Blair, B. Bland, T. P. Bodiya, L. Bogue, R. Bork, V. Boschi, S. Bose, P. R. Brady, V. B. Braginsky, J. E. Brau, D. O. Bridges, M. Brinkmann, A. F. Brooks, D. A. Brown, A. Brummit, G. Brunet, A. Bullington, A. Buonanno, O. Burmeister, R. L. Byer, L. Cadonati, J. B. Camp, J. Cannizzo, K. C. Cannon, J. Cao, L. Cardenas, S. Caride, G. Castaldi, S. Caudill, M. Cavaglia, C. Cepeda, T. Chalmersongsak, E. Chalkley, P. Charlton, S. Chatterji, S. Chelkowsky, Y. Chen, N. Christensen, C. T. Y. Chung, D. Clark, J. Clark, J. H. Clayton, T. Cokelaer, C. N. Colacino, R. Conte, D. Cook, T. R. C. Corbitt, N. Cornish, D. Coward, D. C. Coyne, J. D. E. Creighton, T. D. Creighton, A. M. Cruise, R. M. Culter, A. Cumming, L. Cunningham, S. L. Danilishin, K. Danzmann, B. Daudert, G. Davies, E. J. Daw, D. DeBra, J. Degallaix, V. Dergachev, S. Desai, R. DeSalvo, S. Dhurandhar, M. Díaz, A. Dietz, F. Donovan, K. L. Dooley, E. E. Doomes, R. W. P. Drever, J. Dueck, I. Duke, J.-C. Dumas, J. G. Dwyer, C. Echols, M. Edgar, A. Effler, P. Ehrens, E. Espinoza, T. Etzel, M. Evans, T. Evans, S. Fairhurst, Y. Faltas, Y. Fan, D. Fazi, H. Fehrmann, L. S. Finn, K. Flasch, S. Foley, C. Forrest, N. Fotopoulos, A. Franzen, M. Frede, M. Frei, Z. Frei, A. Freise, R. Frey, T. Fricke, P. Fritschel, V. V. Frolov, M. Fyffe, V. Galdi, J. A. Garofoli, I. Gholami, J. A. Giaime, S. Giampanis, K. D. Giardina, K. Goda, E. Goetz, L. M. Goggin, G. González, M. L. Gorodetsky, S. Goßler, R. Gouaty, A. Grant, S. Gras, C. Gray, M. Gray, R. J. S. Greenhalgh, A. M. Gretarsson, F. Grimaldi, R. Grosso, H. Grote, S. Grunewald, M. Guenther, E. K. Gustafson, R. Gustafson, B. Hage, J. M. Hallam, D. Hammer, G. D. Hammond, C. Hanna, J. Hanson, J. Harms, G. M. Harry, I. W. Harry, E. D. Harstad, K. Haughian, K. Hayama, J. Heefner, I. S. Heng, A. Heptonstall, M. Hewitson, S. Hild, E. Hirose, D. Hoak, K. A. Hodge, K. Holt, D. J. Hosken, J. Hough, D. Hoyland, B. Hughey, S. H. Huttner, D. R. Ingram, T. Isogai, M. Ito, A. Ivanov, B. Johnson, W. W. Johnson, D. I. Jones, G. Jones, R. Jones, L. Ju, P. Kalmus, V. Kalogera, S. Kandhasamy, J. Kanner, D. Kasprzyk, E. Katsavounidis, K. Kawabe, S. Kawamura, F. Kawazoe, W. Kells, D. G. Keppel, A. Khalaidovski, F. Y. Khalili, R. Khan, E. Khazanov, P. King, J. S. Kissel, S. Klimentko, K. Kokeyama, V. Kondrashov, R. Koppalapu, S. Koranda, D. Kozak, B. Krishnan, R. Kumar, P. Kwee, P. K. Lam, M. Landry, B. Lantz, A. Lazzarini, H. Lei, M. Lei, N. Leindegger, I. Leonor, C. Li, H. Lin, P. E. Lindquist, T. B. Littenberg, N. A. Lockerbie, D. Lodhia, M. Longo, M. Lormand, P. Lu, M. Lubinski, A. Lucianetti, H. Lück, B. Machenschalk, M. MacInnis, M. Mageswaran, K. Mäkelä, I. Mandel, V. Mandic, S. Márka, Z. Márka, A. Markosyan, J. Markowitz, E. Maros, I. W. Martin, R. M. Martin, J. N. Marx, K. Mason, F. Matichard, L. Matone, R. A. Matzner, N. Mavalvala, R. McCarthy, D. E. McClelland, S. C. McGuire, M. McHugh, G. McIntyre, D. J. A. McKechnan, K. McKenzie, M. Mehmet, A. Melatos, A. C. Melissinos, D. F. Menéndez, G. Mendell, R. A. Mercer, S. Meshkov, C. Messenger, M. S. Meyer, J. Miller, J. Minelli, Y. Mino, V. P. Mitrofanov, G. Mitselmakher, R. Mittleman, O. Miyakawa, B. Moe, S. D. Mohanty, S. R. P. Mohapatra, G. Moreno, T. Morioka, K. Mors, K. Mossavi, C. MowLowry, G. Mueller, H. Müller-Ebhardt, D. Muhammad, S. Mukherjee, H. Mukhopadhyay, A. Mullavey, J. Munch, P. G. Murray, E. Myers, J. Myers, T. Nash, J. Nelson, G. Newton, A. Nishizawa, K. Numata, J. O'Dell, B. O'Reilly, R. O'Shaughnessy, E. Ochsner, G. H. Ogin, D. J. Ottaway, R. S. Ottens, H. Overmier, B. J. Owen, Y. Pan, C. Pankow, M. A. Papa, V. Parameshwaraiah, P. Patel, M. Pedraza, S. Penn, A. Perraca, V. Pierro, I. M. Pinto, M. Pitkin, H. J. Pletsch, M. V. Plissi, F. Postiglione, M. Principe, R. Prix, L. Prokhorov, O. Punken, V. Quetschke, F. J. Raab, D. S. Rabeling, H. Radkins, P. Raffai, Z. Raics, N. Rainer, M. Rakhmanov, V. Raymond, C. M. Reed, T. Reed, H. Rehbein, S. Reid, D. H. Reitze, R. Riesen, K. Riles, B. Rivera, P. Roberts, N. A. Robertson, C. Robinson, E. L. Robinson, S. Roddy, C. Röver, J. Rollins, J. D. Romano, J. H. Romie, S. Rowan, A. Rüdiger, P. Russell, K. Ryan, S. Sakata, L. S. de la Jordana, V. Sandberg, V. Sannibale, L. Santamaría, S. Saraf, P. Sarin, B. S. Sathyaprakash, S. Sato, M. Satterthwaite, P. R. Saulson, R. Savage, P. Savov, M. Scanlan, R. Schilling, R. Schnabel, R. Schofield, B. Schulz, B. F. Schutz, P. Schwinberg, J. Scott, S. M. Scott, A. C. Searle, B. Sears, F. Seifert, D. Sellers, A. S. Sengupta, A. Sergeev, B. Shapiro, P. Shawhan, D. H. Shoemaker, A. Sibley, X. Siemens, D. Sigg, S. Sinha, A. M. Sintes, B. J.

- J. Slagmolen, J. Slutsky, J. R. Smith, M. R. Smith, N. D. Smith, K. Somiya, B. Sorazu, A. Stein, L. C. Stein, S. Stepleski, A. Stochino, R. Stone, K. A. Strain, S. Strigin, A. Stroerer, A. L. Stuver, T. Z. Summerscales, K.-X. Sun, M. Sung, P. J. Sutton, G. P. Szokoly, D. Talukder, L. Tang, D. B. Tanner, S. P. Tarabrin, J. R. Taylor, R. Taylor, J. Thacker, K. A. Thorne, A. Thüring, K. V. Tokmakov, C. Torres, C. Torrie, G. Traylor, M. Trias, D. Ugolini, J. Ulmen, K. Urbanek, H. Vahlbruch, M. Vallisneri, C. V. D. Broeck, M. V. van der Sluys, A. A. van Veggel, S. Vass, R. Vaulin, A. Vecchio, J. Veitch, P. Veitch, C. Veltkamp, A. Villar, C. Vorvick, S. P. Vyachanin, S. J. Waldman, L. Wallace, R. L. Ward, A. Weidner, M. Weinert, A. J. Weinstein, R. Weiss, L. Wen, S. Wen, K. Wette, J. T. Whelan, S. E. Whitcomb, B. F. Whiting, C. Wilkinson, P. A. Willems, H. R. Williams, L. Williams, B. Willke, I. Wilmot, L. Winkelmann, W. Winkler, C. C. Wipf, A. G. Wiseman, G. Woan, R. Wooley, J. Worden, W. Wu, I. Yakushin, H. Yamamoto, Z. Yan, S. Yoshida, M. Zanolin, J. Zhang, L. Zhang, C. Zhao, N. Zotov, M. E. Zucker, H. zur Mühlen, and J. Zweigig, "LIGO: the Laser Interferometer Gravitational-Wave Observatory," *Rep. Prog. Phys.* **72**, 076901 (2009).
5. A. Sathe, J. Mann, J. Gottschall, and M. S. Courtney, "Can Wind Lidars Measure Turbulence?" *J. Atmospheric Ocean. Technol.* **28**, 853–868 (2011).
 6. X. Liu, X. Zhang, X. Zhai, H. Zhang, B. Liu, and S. Wu, "Observation of Aircraft Wake Vortex Evolution under Crosswind Conditions by Pulsed Coherent Doppler Lidar," *Atmosphere* **12**(1), 49 (2021).
 7. W. Abdalati, H. J. Zwally, R. Bindschadler, B. Csatho, S. L. Farrell, H. A. Fricker, D. Harding, R. Kwok, M. Lefsky, T. Markus, A. Marshak, T. Neumann, S. Palm, B. Schutz, B. Smith, J. Spinhirne, and C. Webb, "The ICESat-2 Laser Altimetry Mission," *Proc. IEEE* **98**(5), 735–751 (2010).
 8. W. Drexler and J. G. Fujimoto, eds., *Optical Coherence Tomography* (Springer International Publishing, 2015).
 9. C. Rosales-Guzmán, N. Hermosa, A. Belmonte, and J. P. Torres, "Measuring the translational and rotational velocities of particles in helical motion using structured light," *Opt. Express* **22**(13), 16504 (2014).
 10. N. Bobroff, "Recent advances in displacement measuring interferometry," *Meas. Sci. Technol.* **4**(9), 907–926 (1993).
 11. R. Pierce, J. Leitch, M. Stephens, P. Bender, and R. Nerem, "Intersatellite range monitoring using optical interferometry," *Appl. Opt.* **47**(27), 5007 (2008).
 12. D. Kucharski, G. Kirchner, F. Koidl, C. Fan, R. Carman, C. Moore, A. Dmytrotsa, M. Ploner, G. Bianco, M. Medvedskij, A. Makeyev, G. Appleby, M. Suzuki, J.-M. Torre, Z. Zhongping, L. Grunwaldt, and Q. Feng, "Attitude and Spin Period of Space Debris Envisat Measured by Satellite Laser Ranging," *IEEE Trans. Geosci. Remote Sens.* **52**(12), 7651–7657 (2014).
 13. K. Minoshima and H. Matsumoto, "High-accuracy measurement of 240-m distance in an optical tunnel by use of a compact femtosecond laser," *Appl. Opt.* **39**(30), 5512 (2000).
 14. I. Coddington, W. C. Swann, L. Nenadovic, and N. R. Newbury, "Rapid and precise absolute distance measurements at long range," *Nat. Photonics* **3**(6), 351–356 (2009).
 15. J. Lee, S. Han, K. Lee, E. Bae, S. Kim, S. Lee, S.-W. Kim, and Y.-J. Kim, "Absolute distance measurement by dual-comb interferometry with adjustable synthetic wavelength," *Meas. Sci. Technol.* **24**(4), 045201 (2013).
 16. Z. Zhu, G. Xu, K. Ni, Q. Zhou, and G. Wu, "Synthetic-wavelength-based dual-comb interferometry for fast and precise absolute distance measurement," *Opt. Express* **26**(5), 5747 (2018).
 17. T.-A. Liu, N. R. Newbury, and I. Coddington, "Sub-micron absolute distance measurements in sub-millisecond times with dual free-running femtosecond Er fiber-lasers," *Opt. Express* **19**(19), 18501 (2011).
 18. T. Fortier and E. Baumann, "20 years of developments in optical frequency comb technology and applications," *Commun. Phys.* **2**(1), 153 (2019).
 19. Y.-S. Jang and S.-W. Kim, "Distance Measurements Using Mode-Locked Lasers: A Review," *Nanomanufacturing Metrol.* **1**(3), 131–147 (2018).
 20. Z. Zhu and G. Wu, "Dual-Comb Ranging," *Engineering* **4**(6), 772–778 (2018).
 21. D. Hu, Z. Wu, H. Cao, Y. Shi, R. Li, H. Tian, Y. Song, and M. Hu, "Dual-comb absolute distance measurement of non-cooperative targets with a single free-running mode-locked fiber laser," *Opt. Commun.* **482**, 126566 (2021).
 22. Z. Zhu, K. Ni, Q. Zhou, and G. Wu, "Two-color phase-stable dual-comb ranging without precise environmental sensing," *Opt. Express* **27**(4), 4660 (2019).
 23. H. Wright, J. Sun, D. McKendrick, N. Weston, and D. T. Reid, "Two-photon dual-comb LiDAR," *Opt. Express* **29**(23), 37037 (2021).
 24. P. Trocha, M. Karpov, D. Ganin, M. H. P. Pfeiffer, A. Kordts, S. Wolf, J. Krockenberger, P. Marin-Palomo, C. Weimann, S. Randel, W. Freude, T. J. Kippenberg, and C. Koos, "Ultrafast optical ranging using microresonator soliton frequency combs," *Science* **359**(6378), 887–891 (2018).
 25. J. E. Morales, J. Kim, and R. R. Richardson, "Gyroless Spin-Stabilization Controller and Deorbiting Algorithm for CubeSats," *Int. J. Aeronaut. Space Sci.* **22**(2), 445–455 (2021).
 26. O. Mori and S. Matunaga, "Formation and Attitude Control for Rotational Tethered Satellite Clusters," *J. Spacecr. Rockets* **44**(1), 211–220 (2007).
 27. M. Y. Ovchinnikov, V. I. Penkov, D. S. Roldugin, and S. S. Tkachev, "Single axis stabilization of a fast rotating satellite in the orbital frame using magnetorquers and a rotor," *Acta Astronaut.* **173**, 195–201 (2020).
 28. S.-I. Nishida, S. Kawamoto, Y. Okawa, F. Terui, and S. Kitamura, "Space debris removal system using a small satellite," *Acta Astronaut.* **65**(1-2), 95–102 (2009).
 29. V. C. Ravindra, Y. Bar-Shalom, and P. Willett, "Projectile Identification and Impact Point Prediction," *IEEE Trans. Aerosp. Electron. Syst.* **46**(4), 2004–2021 (2010).

30. E. P. Hassel and S. Linow, "Laser diagnostics for studies of turbulent combustion," *Meas. Sci. Technol.* **11**(2), R37–R57 (2000).
31. E. Bou, A. Ly, J. Roul, O. Llopis, C. Vieu, and A. Cerf, "Compact system for in situ laser Doppler velocimetry of blood flow," *Biomed. Opt. Express* **10**(11), 5862 (2019).
32. S. Han, Y.-J. Kim, and S.-W. Kim, "Parallel determination of absolute distances to multiple targets by time-of-flight measurement using femtosecond light pulses," *Opt. Express* **23**(20), 25874 (2015).
33. Y. Watanabe, T. Komuro, S. Kagami, and M. Ishikawa, "Real-time visual measurements using high-speed vision," *SPIE Digital Library Proceedings* 5603 (2004).
34. M. P. J. Lavery, F. C. Speirits, S. M. Barnett, and M. J. Padgett, "Detection of a Spinning Object Using Light's Orbital Angular Momentum," *Science* **341**(6145), 537–540 (2013).
35. H. Zhou, D. Fu, J. Dong, P. Zhang, and X. Zhang, "Theoretical analysis and experimental verification on optical rotational Doppler effect," *Opt. Express* **24**(9), 10050 (2016).
36. L. Allen, M. W. Beijersbergen, R. J. C. Spreeuw, and J. P. Woerdman, "Orbital angular momentum of light and the transformation of Laguerre-Gaussian laser modes," *Phys. Rev. A* **45**(11), 8185–8189 (1992).
37. M. P. J. Lavery, S. M. Barnett, F. C. Speirits, and M. J. Padgett, "Observation of the rotational Doppler shift of a white-light, orbital-angular-momentum-carrying beam backscattered from a rotating body," *Optica* **1**(1), 1 (2014).
38. A. Ryabtsev, S. Pouya, A. Safaripour, M. Koochesfahani, and M. Dantus, "Fluid flow vorticity measurement using laser beams with orbital angular momentum," *Opt. Express* **24**(11), 11762 (2016).
39. E. F. Strong, A. Q. Anderson, M. P. Brenner, B. M. Heffernan, N. Hoghooghi, J. T. Gopinath, and G. B. Rieker, "Angular velocimetry for fluid flows: an optical sensor using structured light and machine learning," *Opt. Express* **29**(7), 9960–9980 (2021).
40. A. Belmonte, C. Rosales-Guzmán, and J. P. Torres, "Measurement of flow vorticity with helical beams of light," *Optica* **2**(11), 1002 (2015).
41. A. Q. Anderson, E. F. Strong, B. M. Heffernan, M. E. Siemens, G. B. Rieker, and J. T. Gopinath, "Detection technique effect on rotational Doppler measurements," *Opt. Lett.* **45**(9), 2636 (2020).
42. R. Neo, S. Leon-Saval, J. Bland-Hawthorn, and G. Molina-Terriza, "OAM interferometry: the detection of the rotational Doppler shift," *Opt. Express* **25**(18), 21159 (2017).
43. S. Xiao, L. Zhang, D. Wei, F. Liu, Y. Zhang, and M. Xiao, "Orbital Angular Momentum-Enhanced Measurement of Rotation Vibration Using a Sagnac Interferometer," *Opt. Express* **26**(2), 1997–2005 (2018).
44. J. Guo, S. Ming, Y. Wu, L. Q. Chen, and W. Zhang, "Super-sensitive rotation measurement with an orbital angular momentum atom-light hybrid interferometer," *Opt. Express* **29**(1), 208–218 (2021).
45. Z. Zhang, L. Cen, F. Wang, and Y. Zhao, "Tiny velocity measurement using rotating petal-like mode of orbital angular momentum," *Opt. Lett.* **46**(19), 4805–4808 (2021).
46. W. Zhang, J. Gao, D. Zhang, Y. He, T. Xu, R. Fickler, and L. Chen, "Free-Space Remote Sensing of Rotation at the Photon-Counting Level," *Phys. Rev. Appl.* **10**(4), 044014 (2018).
47. A. Belmonte and J. P. Torres, "Optical Doppler shift with structured light," *Opt. Lett.* **36**(22), 4437–4439 (2011).
48. Y. Zhai, S. Fu, R. Zhang, C. Yin, H. Zhou, J. Zhang, and C. Gao, "The radial Doppler effect of optical vortex beams induced by a surface with radially moving periodic structure," *J. Opt.* **21**(5), 054002 (2019).
49. C. Dorrer, D. C. Kilper, H. R. Stuart, G. Raybon, and M. G. Raymer, "Linear optical sampling," *IEEE Photonics Technol. Lett.* **15**(12), 1746–1748 (2003).
50. B. Jack, M. J. Padgett, and S. Franke-Arnold, "Angular diffraction," *New J. Phys.* **10**(10), 103013 (2008).
51. L. Torner, J. P. Torres, and S. Carrasco, "Digital spiral imaging," *Opt. Express* **13**(3), 873–881 (2005).
52. O. Emile, J. Emile, and C. Brousseau, "Rotational Doppler shift upon reflection from a right angle prism," *Appl. Phys. Lett.* **116**(22), 221102 (2020).
53. D. Petrov, N. Rahuel, G. Molina-Terriza, and L. Torner, "Characterization of dielectric spheres by spiral imaging," *Opt. Lett.* **37**(5), 869 (2012).
54. H.-L. Zhou, D.-Z. Fu, J.-J. Dong, P. Zhang, D.-X. Chen, X.-L. Cai, F.-L. Li, and X.-L. Zhang, "Orbital angular momentum complex spectrum analyzer for vortex light based on the rotational Doppler effect," *Light: Sci. Appl.* **6**(4), e16251 (2017).
55. I. Coddington, W. Swann, and N. Newbury, "Coherent dual-comb spectroscopy at high signal-to-noise ratio," *Phys. Rev. A* **82**(4), 043817 (2010).
56. G. Wu, Q. Zhou, L. Shen, K. Ni, X. Zeng, and Y. Li, "Experimental optimization of the repetition rate difference in dual-comb ranging system," *Appl. Phys. Express* **7**(10), 106602 (2014).
57. Z. Ding, Y. Zhao, H. Ren, J. S. Nelson, and Z. Chen, "Real-time phase-resolved optical coherence tomography and optical Doppler tomography," *Opt. Express* **10**(5), 236 (2002).
58. M. V. Sarunic, B. E. Applegate, and J. A. Izatt, "Real-time quadrature projection complex conjugate resolved Fourier domain optical coherence tomography," *Opt. Lett.* **31**(16), 2426 (2006).
59. M. A. Choma, C. Yang, and J. A. Izatt, "Instantaneous quadrature low-coherence interferometry with 3×3 fiber-optic couplers," *Opt. Lett.* **28**(22), 2162 (2003).
60. K. H. Rosen, *Elementary Number Theory and Its Applications*. (Addison-Wesley, 1984).
61. C. Wang, Q. Yin, and H. Chen, "Robust Chinese Remainder Theorem Ranging Method Based on Dual-Frequency Measurements," *IEEE Trans. Veh. Technol.* **60**(8), 4094–4099 (2011).

62. X.-G. Xia and G. Wang, "Phase Unwrapping and A Robust Chinese Remainder Theorem," *IEEE Signal Process. Lett.* **14**(4), 247–250 (2007).
63. L. C. Sinclair, I. Coddington, W. C. Swann, G. B. Rieker, A. Hati, K. Iwakuni, and N. R. Newbury, "Operation of an optically coherent frequency comb outside the metrology lab," *Opt. Express* **22**(6), 6996 (2014).
64. L. C. Sinclair, J.-D. Deschênes, L. Sonderhouse, W. C. Swann, I. H. Khader, E. Baumann, N. R. Newbury, and I. Coddington, "Invited Article: A compact optically coherent fiber frequency comb," *Rev. Sci. Instrum.* **86**(8), 081301 (2015).
65. G.-W. Truong, E. M. Waxman, K. C. Cossel, E. Baumann, A. Klose, F. R. Giorgetta, W. C. Swann, N. R. Newbury, and I. Coddington, "Accurate frequency referencing for fieldable dual-comb spectroscopy," *Opt. Express* **24**(26), 30495 (2016).
66. S. Coburn, C. B. Alden, R. Wright, K. Cossel, E. Baumann, G.-W. Truong, F. Giorgetta, C. Sweeney, N. R. Newbury, K. Prasad, I. Coddington, and G. B. Rieker, "Regional trace-gas source attribution using a field-deployed dual frequency comb spectrometer," *Optica* **5**(4), 320 (2018).
67. T. W. Clark, R. F. Offer, S. Franke-Arnold, A. S. Arnold, and N. Radwell, "Comparison of beam generation techniques using a phase only spatial light modulator," *Opt. Express* **24**(6), 6249 (2016).
68. Z. Zhu, G. Xu, K. Ni, Q. Zhou, and G. Wu, "Improving the accuracy of a dual-comb interferometer by suppressing the relative linewidth," *Meas. Sci. Technol.* **29**(4), 045007 (2018).
69. Z. Zhu, K. Ni, Q. Zhou, and G. Wu, "Digital correction method for realizing a phase-stable dual-comb interferometer," *Opt. Express* **26**(13), 16813 (2018).
70. T. Ideguchi, A. Poisson, G. Guelachvili, N. Picqué, and T. W. Hänsch, "Adaptive real-time dual-comb spectroscopy," *Nat. Commun.* **5**(1), 3375 (2014).
71. Z. Chen, M. Yan, T. W. Hänsch, and N. Picqué, "A phase-stable dual-comb interferometer," *Nat. Commun.* **9**(1), 3035 (2018).
72. J. Roy, J.-D. Deschênes, S. Potvin, and J. Genest, "Continuous real-time correction and averaging for frequency comb interferometry," *Opt. Express* **20**(20), 21932 (2012).
73. D. M. B. Lesko, A. J. Lind, N. Hoghooghi, A. Kowligy, H. Timmers, P. Sekhar, B. Rudin, F. Emaury, G. B. Rieker, and S. A. Diddams, "Fully phase-stabilized 1 GHz turnkey frequency comb at 1.56 μm ," *OSA Contin.* **3**(8), 2070 (2020).
74. D. Kwon, I. Jeon, W.-K. Lee, M.-S. Heo, and J. Kim, "Generation of multiple ultrastable optical frequency combs from an all-fiber photonic platform," *Sci. Adv.* **6**(13), eaax4457 (2020).
75. Y. Ma, B. Xu, H. Ishii, F. Meng, Y. Nakajima, I. Matsushima, T. R. Schibli, Z. Zhang, and K. Minoshima, "Low-noise 750 MHz spaced ytterbium fiber frequency combs," *Opt. Lett.* **43**(17), 4136 (2018).